New Methodology Shows Short Atmospheric Lifetimes of Oxidized Sulfur and Nitrogen due to Dry Deposition

Katherine Hayden[1], Shao-Meng Li[1,2*], Paul Makar[1], John Liggio[1], Samar G. Moussa[1], Ayodeji Akingunola[1], Robert McLaren[3], Ralf M. Staebler[1], Andrea Darlington[1], Jason O'Brien[1], Junhua Zhang[1], Mengistu Wolde[4], Leiming Zhang[1]

[1]*Air Quality Research Division, Environment and Climate Change Canada, Toronto, Ontario, Canada, M3H 5T4*

[2]*College of Environmental Science and Engineering, Peking University, Beijing 100871 China*

[3]*Center for Atmospheric Chemistry, York University, 4700 Keele Street, Toronto, Ontario, Canada*

[4]*National Research Council Canada, Flight Research Laboratory, Ottawa, Canada K1A 0R6*

*corresponding authors shaomeng.li@pku.edu.cn; Katherine.hayden@canada.ca

For submission to *Atmospheric Chemistry and Physics*

Abstract

The atmospheric lifetimes of pollutants determine their impacts on human health, ecosystems and climate and yet, pollutant lifetimes due to dry deposition over large regions have not been determined from measurements. Here, a new methodology based on aircraft observations is used to determine the lifetimes of oxidized sulfur and nitrogen due to dry deposition over (3-6)x10^3 km^2 of boreal forest in Canada. Dry deposition fluxes decreased exponentially with distance from the Athabasca oil sands sources, located in northern Alberta, resulting in lifetimes of 2.2-26 hours. Fluxes were 2-14 and 1-18 times higher than model estimates for oxidized sulfur and nitrogen, respectively, indicating dry deposition velocities which were 1.2-5.4 times higher than those computed for models. A Monte-Carlo analysis with five commonly used inferential dry deposition algorithms indicates that such model underestimates of dry deposition velocity are typical. These findings indicate that deposition to vegetation surfaces are likely under-estimated in regional and global chemical transport models regardless of the model algorithm used. The model-observation gaps may be reduced if surface pH, and quasi-laminar and aerodynamic resistances in algorithms are optimized as shown in the Monte-Carlo analysis. Assessing the air quality and climate impacts of atmospheric pollutants on regional and global scales requires improved measurement-based understanding of atmospheric lifetimes of these pollutants.

1 Introduction

Deposition represents the terminating process for most air pollutants and the starting point for ecosystem impacts. Understanding deposition is critical in determining the atmospheric lifetimes and spatial scale of atmospheric transport of pollutants, which in turn, dictates their ecosystem (WHO, 2016; Solomon et al., 2007) and climate (Samset et al., 2014) impacts. In particular, atmospheric lifetimes ($\boldsymbol{\tau}$) of oxidized sulfur and nitrogen compounds influence their concentrations and column burdens in air, which affect air quality and hence human exposure (WHO, 2016). Furthermore, the lifetime of these species affects their contributions to atmospheric aerosols, with a consequent influence on climate via changes to radiative transfer through scattering and cloud formation (Solomon et al., 2007). In addition, their deposition can exceed critical load thresholds causing aquatic and terrestrial acidification, and eutrophication in the case of nitrogen deposition (Howarth, 2008; Bobbink et al., 2010; Doney, 2010; Vet et al., 2014; Wright et al., 2018). Quantifying $\boldsymbol{\tau}$ and deposition thus provides a crucial assessment of these regional and global impacts.

Deposition occurs through wet and dry processes. While wet deposition fluxes can be measured directly (Vet et al., 2014), there are few validated methods for dry deposition fluxes (Wesley and Hicks, 2000), and none which estimates deposition over large regions. Dry deposition fluxes ($\boldsymbol{F}$) may be obtained using micrometeorological measurements for pollutants for which fast response instruments are available. However, these results are only valid for the footprints of the observation sites, typically hundreds of meters (Aubinet e al., 2012), and their extrapolation to larger regions may suffer from representativeness issues. As a result, atmospheric lifetimes $\boldsymbol{\tau}$ with respect to dry deposition have not been determined through direct observations. On a regional scale, dry deposition fluxes are typically derived using an inferential

approach by multiplying network-measured or model-predicted air concentrations with dry deposition velocities ($\boldsymbol{V_d}$) (Sickles and Shadwick, 2015; Fowler et al., 2009; Meyers et al., 1991), which are derived using resistance-based inferential dry deposition algorithms (Wu et al., 2018), and compared with limited micrometeorological flux measurements (Wesley and Hicks, 2000; Wu et al., 2018; Finkelstein et al., 2000; Matsuda et al., 2006; Makar et al., 2018) for validation. When applied to a regional scale, an inferential-algorithm derived $\boldsymbol{V_d}$ may have significant uncertainties (Wesley and Hicks, 2000; Aubinet et al., 2012;Wu et al., 2018; Finkelstein et al., 2000; Matsuda et al., 2006; Makar et al., 2018; Brook et al., 1997). For example, inferred $\boldsymbol{V_d}$ for SO_2, despite being the most studied and best estimated, may be underestimated by 35% for forest canopies (Finkelstein et al., 2000). Underestimated $\boldsymbol{V_d}$ for SO_2 and nitrogen oxides can contribute to model over-prediction of regional and global SO_2 concentrations (Solomon et al., 2007; Christian et al., 2015; Chin et al., 2000), or under-prediction of global oxidized nitrogen dry deposition fluxes (Paulot et al., 2018; Dentener et al., 2006).

Here, a new approach is presented to determine $\boldsymbol{\tau}$ with respect to dry deposition and $\boldsymbol{F}$ for total oxidized sulfur (**TOS**, the sulfur mass in SO_2 and particle-SO_4 (pSO_4)) and total reactive oxidized nitrogen (**TON**, the nitrogen mass in NO, NO_2, and others designated as NO_z) on a spatial scale of (3-6)x10^3 km^2, using aircraft measurements. This approach provides a unique methodology to determine $\boldsymbol{\tau}$ and $\boldsymbol{F}$ over a large region. Coupled with analyses for chemical reaction rates (for **TOS** compounds), the average $\boldsymbol{V_d}$ for **TOS** and **TON** over the same spatial scale were also determined. The airborne measurements were obtained during an intensive campaign from August to September 2013 in the ~~A~~Athabasca Oil Sands Region (AOSR) (Gordon et al., 2015; Liggio et al., 2016; Li et al., 2017; Baray et al., 2018; Liggio et al., 2019) in

northern Alberta, Canada. Direct comparisons with modelled dry deposition estimates are made to assess their uncertainties and the spatial-temporal scales of air pollutant impacts.

2 Methods

2.1 Lagrangian Flight Design

Details of the airborne measurement program have been described elsewhere (Gordon et al., 2015; Liggio et al., 2016; Li et al., 2017; Liggio et al., 2019; Baray et al., 2018). Briefly, an instrumented National Research Council of Canada's Convair-580 research aircraft was flown over the ~~Athabasca oil sands region (~~AOSR~~)~~ in Alberta, Canada from August 13 to September 7, 2013. The flights were designed to determine emissions from mining activities in the AOSR, assess their atmospheric transformation processes and gather data for satellite and numerical model validation. Three flights were flown to study transformation and deposition processes by flying a Lagrangian pattern so that the same pollutant air mass was sampled at different time intervals downwind of emission sources for a total of 4-5 hours and up to 107-135 km downwind of the AOSR sources. Flights 7 (F7, Aug 19), 19 (F19, Sep 4) and 20 (F20, Sep 5) took place during the afternoon when the boundary layer was well established. The flights were conducted in clear sky conditions so wet deposition processes were insignificant. As shown in Figure 1, t~~T~~he aircraft flew tracks perpendicular to the oil sands plume at multiple altitudes between 150 to 1400 m agl and multiple intercepts of the same plume downwind. Vertical profiles conducted as spirals were flown at the centre of the plume which provided information on the boundary layer height and extent of plume mixing. The flight tracks closest to the AOSR intercepted the main emissions from the oil sands operations; t~~T~~here were no other anthropogenic sources as the aircraft flew further downwind of the AOSR.

2.2 Aircraft Measurements

A comprehensive suite of detailed gas- and particle-phase measurements were made from the aircraft. Measurements pertaining to the analysis in this paper are discussed below.

SO_2 and NO_y. Ambient air was drawn in through a 6.35 mm (1/4") diameter PFA sampling line taken from a rear-facing inlet located on the roof towards the rear of the aircraft. The inlet was pressure-controlled to 770 mm Hg using a combination of a MKS pressure controller and a Teflon pump. Ambient air from the pressure-controlled inlet was fed to instrumentation for measuring SO_2 and NO_y. The total sample flow rate was measured at 4988 cm^3 min^{-1} of which SO_2 and NO_y were 429 and 1085 cm^3 min^{-1}, respectively. SO_2 was detected via pulsed fluorescence with a Thermo 43iTLE (Thermo Fisher Scientific, Franklin, MA, USA). NO_y (also denoted as Total Oxidized Nitrogen (TON)) was measured by passing ambient air across a heated (325ºC) molybdenum converter that reduces reactive nitrogen oxide species to NO. NO was then detected through chemiluminescence with a modified Thermo 42iTL (Thermo Fisher Scientific, Franklin, MA, USA) run in NO_y mode. An inlet filter was used for SO_2 to exclude particles, but NO_y was not filtered prior to the molybdenum converter. NO_y includes NO, NO_2, HNO_3 and other oxides of nitrogen such as peroxy acetyl nitrate and organic nitrates (Dunlea et al., 2007; Williams et al., 1998). Although there was no filter on the NO_y inlet to exclude particles, the inlet was not designed to sample particles (i.e. rear-facing PFA tubing). As a result, pNO_3 was not included as part of NO_y (TON). The conversion efficiency of the heated molybdenum converter and inlet transmission was evaluated with NO_2 and HNO_3 and found to be near 100% and >90%, respectively. ~~Other NO_y species are expected to have a be greater conversion efficiency than that of HNO_3.~~ Previous studies conducted by Williams et al. (1998) showed similar molybdenum converter efficiencies including that of n-propyl nitrate near 100%.

Formatted: Superscript
Formatted: Superscript
Formatted: Subscript
Formatted: Subscript
Formatted: Subscript
Formatted: Subscript

Interferences from alkenes or NH_3 were assumed to be negligible (Williams et al., 1998; Dunlea et al. 2007). Species like NO_3 radical and N_2O_5 are expected to be low in concentration as they photolyze quickly during daytime. Zeros were performed 3-5 times per flight for ~~all instruments~~both the SO_2 and NO_y instruments by passing ambient air through an in-line Koby King Jr cartridge for ~5 minutes. For the NO_y measurements pre-reactor zeroes (dynamic instrument zero) were also obtained periodically throughout each flight using either ambient air or a Koby King Jr. air purifier. Multiple calibrations were conducted before, during and after the study using National Institute Standards and Technology reference standards. Data were recorded at a time resolution of 1 second and corrected for a sampling time delay of 1-3 seconds depending on the instrument. Detection limits were determined as 2 times the standard deviation of the values acquired during zeroes; NO_y was 0.09 ppbv and SO_2 was 0.70 ppbv (Table S1).

Aerosols. Multiple aerosol instruments sub-sampled from a forward facing, shrouded, isokinetic particle inlet (Droplet Measurement Technologies, Boulder, CO, USA). A Time-of-Flight High Resolution Aerosol Mass Spectrometer (AMS) (Aerodyne Research Inc.) was used to measure non-refractory submicron aerosol components including pSO_4, pNO_3, pNH_4, and p-organics. Details of the AMS and its operations have been published elsewhere (DeCarlo et al., 2006). The instrument was operated in mass spectrometry V-mode with a sampling time resolution of 10 seconds. Filtered measurements were taken 4-5 times per flight to determine background signals. Detection limits of 0.048, 0.036, 0.235 and 0.236 ug m^{-3} for pSO_4, pNO_3, pNH_4 and p-organics were determined using 3 times the standard deviation of the average of filtered time periods for all flights (Table S1). Ionization efficiency calibrations using monodisperse ammonium nitrate were performed during the study with an uncertainty of ±9%. Data were corrected for a sampling time delay of 10 seconds by comparing with faster response instruments

Formatted: Subscript

Formatted: Subscript

Formatted: Subscript

Formatted: Subscript

Formatted: Line spacing: Double

Formatted: Superscript

e.g. a wing-mounted Forward Scattering Spectrometer Probe Model 300 (FSSP-300) and an in-board Ultra High Sensitivity Absorption Spectrometer (UHSAS) (both from Droplet Measurement Technologies). The FSSP and UHSAS instruments measure particle diameters that range from 3~~2~~00 nm ~~–~~ – 20 µm and 50 nm - 1 µm, respectively. The AMS data were processed using AMS data analysis software (Squirrel, version 1.51H and PIKA, version 1.10H). The~~A~~ particle collection efficiency (CE) of the AMS was determined through comparisons of~~was applied to the data and determined by comparing~~ the total AMS-derived mass with the mass ~~derived~~ estimated from the size distribution measurements ~~from~~ of the UHSAS assuming a density based on the chemical composition. T~~; t~~he ~~collection efficiency~~CE for F7 and F20 was 0.5 for both flights, and for F19 it was 1.0. The CE was applied to all AMS species for the duration of each flight (Figure S1). Since the AMS measures only particle mass < 1 µm (PM_1) in diameter, the mass of SO_4 formed through OH oxidation was scaled upward to account for all particle sizes that H_2SO_4 vapor could potentially condense on. The scaling factor was determined using the surface area ratio of PM_1/PM_{20} from the aircraft particle measurements, assuming that the condensation process is approximately proportional to the surface area. ~~from the aircraft particle measurements~~. PM_1 measurements were from the UHSAS and PM_{20} were from the FSSP300. As the ratio did not vary significantly in the plumes, one single value was used between each set of screens; in F19 the ratio between screens ranged from 0.6 to 0.8, in F20 the ratio ranged from 0.8 to 0.9, and in F7 the ratio ranged from 0.7 to 0.9 (Liggio et al., 2016).

Measurements are discussed in terms of total oxidized sulfur (TOS, the sulfur mass in SO_2 from the Thermo SO_2 instrument and particle-SO_4 (pSO_4) from the AMS instrument) and total

Formatted: Subscript

Formatted: Subscript

Formatted: Subscript

Formatted: Indent: First line: 0 cm

Formatted: Subscript

reactive oxidized nitrogen (TON, the nitrogen mass in reactive oxidized nitrogen species, from the Thermo NO_y instrument, often denoted NO_y).

Volatile Organic Compounds (VOCs). Selected VOCs were used to estimate the OH concentrations used for determining oxidation rates for SO_2. VOCs were measured with a proton transfer reaction time-of-flight mass spectrometer (PTR-ToF-MS, Ionicon Analytik GmbH, Austria) as well as through discrete canister grab samples. The PTR-ToF-MS and its operation, along with the details of the canister sampling and lab analyses during the study were described in detail previously (Li et al., 2017). Briefly, the PTR-ToF-MS used chemical ionization with H_3O^+ as the primary reagent ion. Gases with a proton affinity greater than that of water were protonated in the drift tube. The pressure and temperature of the drift tube region were maintained at a constant 2.15 mbar and 60°C, respectively for an E/N of 141 Td (Townsend, 1 Td=10^{-17} V cm^2). E/N refers to the reduced electric field parameter in the drift tube; E is the electric field and N is the number density of the gas in the drift tube. The E/N ratio can affect the reagent ion distribution in the drift tube and VOC fragmentation (de Gouw and Warneke; 2007). The protonated gases were detected using a high-resolution time of flight mass spectrometer at a time resolution of 2 seconds. Instrumental backgrounds were performed in flight using a custom-built zero-air generating unit. The unit contained a catalytic converter heated to 350°C with a continuous flow of ambient air at a flow rate of one litre per minute. The data were processed using Tofware software (Tofwerk AG). Calibrations were performed on the ground using gas standard mixtures from Ionicon, Apel-Reimer and Scott-Marrin for 22 compounds. The canister samples were collected in pre-cleaned and passivated 3L stainless steel canisters that were subsequently sent to an analytical laboratory for GC-FID/MS analyses for a suite of 150 hydrocarbon compounds.

Formatted: Subscript

Formatted: Superscript

Formatted: Superscript

Meteorology and aircraft state parameters. Meteorological measurements have been described elsewhere (Gordon et al., 2015). In brief, 3-D wind speed and temperature were measured with a Rosemount 858 probe. Dew point was measured with an Edgetech hygrometer and pressure was measured with a DigiQuartz sensor. Aircraft state parameters including positions and altitudes were measured with GPS and a Honeywell HG1700 unit. All meteorological measurements and aircraft state parameters were measured at a 1 s time resolution.

2.3 Mass transfer rates in the atmosphere

Mass transfer rates (***T***) across flight screens (Figure 1) were determined using an extension of the Top-down Emission Rate Retrieval Algorithm (TERRA) developed for emission rate determination using aircraft measurements (Gordon et al., 2015). Briefly, at each plume interception location, the level flight tracks were stacked to create a virtual screen. Background subtracted pollutant concentrations and horizontal wind speeds normal to the screen were interpolated using kriging. The background for SO_2 was ~0 ppb and pSO_4 was 0.2 – 0.3 μg m^{-3} which was subtracted from the pSO_4 measurements before mass transfer rates were calculated (Liggio et al., 2016). Integration of the horizontal fluxes across the plume extent on the screen yields the transfer rate ***T*** in units of t hr^{-1}. Using SO_2 as an example,

$$T_{SO_2} = \int_{s_1}^{s_2}\int_{z_1}^{z_2} C(s,z)u_n(s,z)dsdz \quad (1)$$

where $C(s,z)$ is the background subtracted concentration at screen coordinate s and z, which represent the horizontal and vertical axes of the screen. The $u_n(s,z)$ is the horizontal wind speed normal to the screen at the same coordinates.

Formatted: Superscript

Since the lowest flight altitude was 150 magl, it was necessary to extrapolate the data to the surface as per the procedures described previously (Gordon et al., 2015). Extrapolation to the surface methods were compared and differences were included in the uncertainty estimates. The main sources of SO_2 were from elevated facility stacks associated with the desulfurization of the raw bitumen (Zhang et al., 2018). The stacks with the biggest SO_2 emissions range in height from 76.2 to 183.0 m. Since the main source of SO_2 is from the elevated facility stacks, the uncertainty for a single screen is estimated at 4% (Gordon et al., 2015). NO_y was also extrapolated linearly to the surface and the mass transfer rates were similarly compared to other extrapolation methods. NO_y sources include the elevated facility stacks and surface sources such as the heavy hauler trucks operating in the surface mines. The uncertainty in the resulting transfer rate ***T*** for a single screen is estimated to be larger at 8%, as a larger fraction of the NO_y mass may be below the lowest measurement altitude (Gordon et al., 2015). Sulfur and nitrogen data were also extrapolated linearly to background values from the highest altitude flight tracks upwards to the mixed layer height, which was determined from vertical profiles of pollutant mixing ratios, temperature and dew point (Table 1).~~). Two different approaches, a finite jump model and a gradient flux approach (Stull, 1988; Degrazia et al., 2015), were used to estimate the potential upward loss across the interface between the boundary layer and the free troposphere for sulfur. In both approaches, the upward S flux was a minor loss at < 45 g /km^{-2}/ hr^{-1}, about 3 orders of magnitude lower than the several to many kg /km^{-2} /hr^{-1} horizontal advectional transport that were determined using TERRA. For N, the upward flux was estimated to be ~570 g km^{-2} hr^{-1}, so although a larger flux than S, it is about factor of 18 lower than the TON fluxes derived from observations.~~

Formatted: Subscript

Formatted: Subscript

Formatted: Not Highlight

Formatted: Superscript

Formatted: Not Highlight

Formatted: Superscript

Formatted: Not Highlight

Formatted: Superscript

Formatted: Not Highlight

Formatted: Superscript

Formatted: Not Highlight

Formatted: Superscript

Formatted: Not Highlight

Formatted: Superscript

Formatted: Not Highlight

Changes in the mass transfer rate $\boldsymbol{T}$ (denoted $\boldsymbol{\Delta T}$) in units of t hr^{-1} were then calculated as the differences in $\boldsymbol{T}$ between pairs of virtual screens. The uncertainty in $\boldsymbol{\Delta T}$ was estimated as 8% for **TOS** and 26% for **TON** as supported by emission rate uncertainties determined for box flights (Gordon et al., 2015). The uncertainty analysis for box flights is applicable to $\boldsymbol{\Delta T}$ here, as both account for uncertainties with an upwind and a downwind screen. The $\boldsymbol{\Delta T}$ uncertainties were propagated through subsequent calculations.

Knowing the change in mass transfer rate $\boldsymbol{\Delta T}$, and accounting for the net rates of chemical loss and formation between screens for SO_2 and pSO_4, the deposition rates (and subsequently the deposition flux in tonnes S (or N) km^{-2} hr^{-1}, Section 2.4 were determined for the sulfur compounds as follows~~, using sulfur compounds as an example~~:

$$\Delta T_{SO_2} = T_{SO_2}(t_2) - T_{SO_2}(t_1) = X_{SO2} - D_{SO2} \quad (2)$$

$$\Delta T_{pSO_4} = T_{pSO_4}(t_2) - T_{pSO4}(t_1) = X_{pSO4} - D_{pSO4} \quad (3)$$

$$\Delta T_{TOS} = T_{TOS}(t_2) - T_{TOS}(t_1) = -D_{TOS} \quad (4)$$

where $\boldsymbol{X_{SO2}}$ is the rate of chemical reaction loss of sulfur mass in SO_2, $\boldsymbol{X_{pSO4}}$ is the rate of chemical formation of sulfur mass as pSO_4, $\boldsymbol{D_{SO2}}$ and $\boldsymbol{D_{pSO4}}$ are deposition rates of sulfur mass in SO_2 and pSO_4 respectively, and t_1 and t_2 are plume interceptions times at Screen 1 and Screen 2, respectively. Note that the chemical loss rate of SO_2 is set to be equivalent to the formation rate of pSO_4 ie. $\boldsymbol{X_{SO2} = X_{pSO4}}$. Equation 4 for TOS can also similarly be written as shown in Equation 5.

$$\Delta T_{TOS} = \Delta T_{SO_2} + \Delta T_{pSO_4} = -D_{SO2} - D_{pSO4} \quad (5)$$

Units in Equations 2 to 5 are all in t hr^{-1}. Reaction with the OH radical was considered to be the most significant chemical loss of SO_2 and the most significant path for the formation of pSO_4.

Formatted: Subscript

Formatted: Subscript

Formatted: Font: Not Italic

Formatted: Not Superscript/ Subscript

~~(further details in SI Section S4.~~ X_{SO2} and X_{pSO4} were determined using estimated OH radical concentrations, which were ~~determined~~ estimated using the methodology described in SI Section S4. Although TON encompasses a range of different N species with expected differences in their deposition rates, it was not possible to quantitatively separate their chemical formation/losses from their deposition rates with this method~~, thus the Dry deposition rates, D_{SO2} and D_{pSO4}, and their uncertainties were determined using Eq. (2) and (3).~~ For total oxidized sulfur **TOS** (i.e., sulfur in SO_2 + pSO_4) and total oxidized nitrogen **TON** (i.e., nitrogen in NO_y) the chemistry term is not relevant, and thus, the dry deposition rate D_{TOS} was directly determined from ΔT_{TOS} using equation (4), and respectively for **TON**.

2.4 Dry deposition fluxes and dry deposition velocities

Average dry deposition fluxes (***F***) for **TOS** and **TON** were obtained by dividing the deposition rates ***D*** in t hr^{-1} with the footprint surface area of the plume between two adjacent screens (Figure 1 grey shaded regions), as shown in Equation ~~6~~5 for the dry deposition flux F_{TOS} of **TOS** (in t S km^{-2} hr^{-1}):

$$F_{TOS} = \frac{D_{TOS}}{Area} \quad (5)$$

where the surface area, *Area*, was identified as the geographic area under the plume extending to the edges of the plume where concentrations fell to background levels (i.e. SO_2 to ~0 ppb; SO_4 ~0.2 ug m^{-3}). This approach was similarly used to derive deposition fluxes from an air quality model, Global Environmental Multiscale – Modelling Air-quality and Chemistry (GEM-MaCH) (Moran et al., 2010; also see SI Section S5 for details). The geographic surface area uncertainty is estimated at 5%. Dry deposition fluxes between the sources and the first screen were also

Formatted: Not Highlight

Formatted: Indent: First line: 0 cm

Formatted: Superscript

Formatted: Superscript

estimated using change in mass transfer rate ΔT based on the extrapolated transfer rates back to the source region ('extended' region). The surface area boundaries for these 'extended' regions were determined using latitude and longitude coordinates that were weighted by emissions. This was done by first using the average wind direction from Screen 1 and creating a set of parallel back trajectories (~20) starting at different parts of Screen 1 back across the source region. For **TON**, the NO_x emission sources along each back trajectory were weighted by their NO_x emissions to obtain an emissions-weighted center location with latitude and longitude coordinates for each back trajectory. The line connecting these emissions-weighted center locations formed the boundary of the extended surface area. The extended surface area was similarly determined for **TOS** based upon the known locations of the major SO_2 point sources. The uncertainty of the 'extended' regions is estimated at 10% based on repeated optimizations of the geographical area. Surface areas are visualized as grey shaded regions between screens in Figure 1 and tabulated in SI Table S1.

Spatially-averaged dry deposition velocities, V_d, based on the aircraft measurements were determined over the surface area between screens using average plume concentrations across pairs of screens at about 40 meters above the ground for ~~**TOS**~~ **SO_2** and **TON** (e.g. Equation 7~~6~~ for SO_2 in units of cm s^{-1}). Although TOS includes the S in both SO_2 and pSO_4, only SO_2 is used in the calculation of V_d since the deposition behaviour of gases and particles differ substantially, and particles additionally have size-dependent deposition rates (Emerson et al., 2020). As the dominant form of TOS is SO_2 (>92%) the deposition behaviour of TOS is expected to be largely driven by that of SO_2. The measured TON does not include pNO_3.

$$V_d = \frac{F_{SO2}}{[SO2]} \qquad (7~~6~~)$$

Formatted: Font: Italic
Formatted: Subscript
Formatted: Not Superscript/ Subscript
Formatted: Superscript
Formatted: Subscript
Formatted: Subscript
Formatted: Subscript
Formatted: Font: Bold, Italic
Formatted: Font: Bold, Italic, Subscript
Formatted: Subscript
Formatted: Subscript
Formatted: Subscript

The largest source of uncertainty in $\boldsymbol{V_d}$ calculated this way was the determination of concentration at 40 meters above the surface as the measurements were extrapolated from the lowest aircraft altitude to the surface and interpolated concentrations were used. The measurement-derived $\boldsymbol{V_d}$ are compared with those from the air quality model GEM-MACH which uses inferential methods.

2.5 Monte-Carlo simulations of dry deposition velocities using multiple resistance-based parameterizations

Parameterization of dry deposition in inferential algorithms is commonly based on a resistance approach with dry deposition velocity depending on three main resistance terms as below:

$$V_d = \frac{1}{R_a + R_b + R_c} \quad (8\text{~~7~~})$$

where R_a, R_b and R_c represent the aerodynamic, quasi-laminar sublayer and bulk surface resistances respectively. Although these resistance terms are common among many regional air quality models (Wu et al., 2018), the formulae used (and inputs in to these formulae) to calculate the individual resistance terms differ significantly among the inferential deposition algorithms. To assess the potential for a general underestimation of $\boldsymbol{V_d}$ across different inferential deposition algorithms, and to compare with the aircraft-derived $\boldsymbol{V_d}$, five different inferential deposition

algorithms, including that used in the GEM-MACH model for calculating $\boldsymbol{V_d}$ (Wu et al., 2018) were incorporated into a Monte-Carlo simulation for $\boldsymbol{V_d}$ for SO_2. NO_y was not considered here, as its measurement includes multiple reactive nitrogen oxide species with different individual deposition velocities. We note that many of the inferential algorithms are based on observations of SO_2 and O_3 deposition made at single sites, and the extent to which a chemical is similar to SO_2 or O_3 features into its $\boldsymbol{V_d}$ calculation – the comparison thus has relevance for species aside from SO_2.

The five deposition algorithms considered are denoted ZHANG, NOAH-GEM, C5DRY, WESLEY and GEM-MACH and are compared in Wu et al. (2018) (except the algorithm in GEM-MACH). The five algorithms all use a big-leaf approach for calculating $\boldsymbol{V_d}$, i.e. $\boldsymbol{V_d}$ is based on the resistance-analogy approach for calculating dry deposition velocity where $\boldsymbol{V_d}$ is the reciprocal sum of three resistance terms R_a, R_b and R_c. Although the approach is similar, the formulations of R_a, R_b and R_c between the algorithms are substantially different (Table 1 in Wu et al., 2018). Results from Wu et al (2018) suggest that the differences in R_a+R_b between different models would cause a difference in their $\boldsymbol{V_d}$ values on the order of 10-30% for most chemical species (including SO_2 and NO_2), although the differences can be much larger for species with near-zero R_c such as HNO_3.

To perform the simulations, formulae for the first four algorithms were taken from Wu et al. (2018) and for GEM-MACH taken from Makar et al. (2018). The stomatal resistance in the ZHANG algorithm was from Zhang et al. (2002). The GEM-MACH formula (Equation 8.7 in the SI of Makar et al. (2018)) for mesophyll resistance R_{mx} contained a typo (missing the Leaf Area Index (LAI)) and was corrected for as follows:

$$R_{mx} = [LAI(H^*/3000 + 100\ f_0)]^{-1} \quad (9)$$

Formatted: Space After: 0 pt, Line spacing: Double
Formatted: Not Highlight
Formatted: Font: 12 pt, Bold, Italic, Not Highlight
Formatted: Font: 12 pt, Bold, Italic, Subscript, Not Highlight
Formatted: Not Highlight
Formatted: Font: 12 pt, Bold, Italic, Not Highlight
Formatted: Font: 12 pt, Bold, Italic, Subscript, Not Highlight
Formatted: Not Highlight
Formatted: Font: 12 pt, Bold, Italic, Not Highlight
Formatted: Font: 12 pt, Bold, Italic, Subscript, Not Highlight
Formatted: Not Highlight
Formatted: Font: 12 pt, Subscript, Not Highlight
Formatted: Not Highlight
Formatted: Font: 12 pt, Subscript, Not Highlight
Formatted: Not Highlight
Formatted: Font: 12 pt, Subscript, Not Highlight
Formatted: Not Highlight
Formatted: Font: 12 pt, Subscript, Not Highlight
Formatted: Not Highlight
Formatted: Font: 12 pt, Subscript, Not Highlight
Formatted: Not Highlight
Formatted: Font: 12 pt, Subscript, Not Highlight
Formatted: Not Highlight
Formatted: Font: 12 pt
Formatted: Not Highlight
Formatted: Font: 12 pt, Subscript, Not Highlight
Formatted: Not Highlight
Formatted: Font: 12 pt, Subscript, Not Highlight
Formatted: Not Highlight
Formatted: Font: 12 pt, Bold, Italic, Not Highlight
Formatted: Font: 12 pt, Bold, Italic, Subscript, Not Highlight
Formatted: Not Highlight
Formatted: Font: 12 pt, Subscript, Not Highlight
Formatted: Not Highlight
Formatted: Font: 12 pt, Subscript, Not Highlight
Formatted: Not Highlight
Formatted: Font: 12 pt, Subscript, Not Highlight
Formatted: Not Highlight
Formatted: Font: 12 pt, Subscript, Not Highlight
Formatted: Not Highlight
Formatted: Font: (Default) Times New Roman, 12 pt

Prescribed input values were constrained by the range of possible values consistent with the conditions during the aircraft flights and are shown in SI Table S3 with associated references. Calculations for the R_a term were based on unstable and dry conditions as observed during the aircraft flights. The Monte-Carlo simulation generated a distribution of possible $\boldsymbol{V_d}$ values, based on randomly generated values of the input variables to each algorithm and selected from Gaussian distributions with a range of 3 sigma for all input parameters. All simulations were performed with the same input values that were common between the algorithms.

3 Results and Discussion

3.1 Meteorological and Emissions Conditions during the Transformation Flights

Three aircraft flights, Flights 7 (F7), 19 (F19) and 20 (F20) were conducted in Lagrangian patterns where the same plume emitted from oil sands activities was repeatedly sampled for a 4-5 hour period and up to 107-135 km downwind of the AOSR. The first screen of each flight captured the main emissions from the oil sands operations with no additional anthropogenic sources between subsequent screens downwind. The main sources of nitrogen oxides were from exhaust emissions from off-road vehicles used in open pit mining activities and sulfur and nitrogen oxides from the elevated facility stack emissions associated with the desulfurization of raw bitumen (Zhang et al., 2018). As depicted in Figure 1, F7 and F19 captured a plume that contained both sulfur and nitrogen oxides. The westerly wind direction and orientation of the aircraft tracks on F20 resulted in the measurement of two distinct plumes; one plume exhibited increased levels of sulfur and nitrogen oxides mainly from the facility stacks, and the other plume contained elevated levels of nitrogen oxides, mainly from the open pit mining activities, and no SO_2.

Formatted: Subscript

During the experiments, the dry deposition rates (***D***) (t hr^{-1}) were quantified under different meteorological conditions and emissions levels of **TOS** and **TON** ($\boldsymbol{E_{TOS}}$ and $\boldsymbol{E_{TON}}$) for the three flights (see Table 1). These differences played important roles in the observed pollutant concentrations and resulting dry deposition fluxes for F7, F19 and F20. Mixed layer heights (MLH) were derived from aircraft vertical profiles that were conducted in the centre of the plume at each downwind set of transects. The profiles of temperature, dew point temperature, relative humidity and pollutant mixing ratios were inspected for vertical gradients indicating a contiguous layer connected to the surface. The highest MLH was determined for F7 at 2500 magl whereas F19 had the lowest MLH at 1200 magl (Table 1). In F20, the MLH was 2100 magl. The combination of a high MLH in F7 with the highest wind speeds resulted in the lowest pollutant concentrations of the three flights. In F19, lower wind speeds and the lowest mixed layer heights led to the highest pollutant levels. F20 had emissions and meteorological conditions that were in between F7 and F19 resulting in pollutant concentrations between those of F7 and F19.

Emission rates of SO_2 and NO_x (designated as $\boldsymbol{E_{TOS}}$ and $\boldsymbol{E_{TON}}$) from the main sources in the AOSR were estimated from the aircraft measurements and varied significantly between the three flight days. The measurement-based emission rates of $\boldsymbol{E_{TOS}}$ and $\boldsymbol{E_{TON}}$ were taken from the mass transfer rates of $\boldsymbol{T_{SO2}}$ and $\boldsymbol{T_{NOy}}$ (described in Methods) by extrapolating backwards to the source locations in the AOSR using exponential functions (Figure 2, Section 3.2). For **TOS**, the source location was set at 57.017N, -111.466W, where the main stacks for SO_2 emissions are located. For **TON**, the source locations were determined from geographically weighted locations. Emission rates $\boldsymbol{E_{TOS}}$ and $\boldsymbol{E_{TON}}$ for each flight are shown in Table 1.

Model-based $\boldsymbol{E_{TOS}}$ and $\boldsymbol{E_{TON}}$ were also obtained from the 2.5 km x 2.5 km gridded emissions fields that were specifically developed for model simulations of the large AOSR surface mining facilities (Zhang et al., 2018) i.e. Suncor Millenium, Syncrude Mildred Lake, Syncrude Aurora North, Shell Canada Muskeg River Mine & Muskeg River Mine Expansion, CNRL Horizon Project and Imperial Kearl Mine. The emissions fields have been used in GEM-MACH (described in SI Section S5) to carry out a number of model simulations (Zhang et al., 2018; Makar et al., 2018) including for the present study. In this work, emissions were summed from various sources including offroad, point (Continuous Emissions Monitoring (CEMS)), and point (non-CEMS) for the surface mines to obtain total AOSR hourly emission rates for the flight time periods of interest (Table 2). The standard deviations reflect the emissions variations during the simulated flight.

3.2 Mass Transfer Rates

The mass transfer rates $\boldsymbol{T}$ (in t hr^{-1}) across the virtual flight screens for all three flights are shown for **TOS** and **TON** in Figure 1 and plotted in Figure 2. In F20, two distinct **TON** plumes were observed, allowing separate $\boldsymbol{T}$ calculations for **TON**. Monotonic decreases in $\boldsymbol{T}$ were observed for both **TOS** and **TON** during transport downwind in all flights, clearly showing dry depositional losses. The deposition rate $\boldsymbol{D}$ (Methods, Section 2.3) was used to estimate the cumulative deposition of **TOS** and **TON** as a fraction of $\boldsymbol{E_{TOS}}$ or $\boldsymbol{E_{TON}}$ and is shown in Figure 3 for F7, F19 and F20 for transport distances of up to 107-135 km downwind of the sources. Curves were fitted to the **TOS** and **TON** dry deposition cumulative percentages from which $\boldsymbol{d_{1/e}}$ and $\boldsymbol{\tau}$ were determined (SI Table S1). The transport e-folding distance ($\boldsymbol{d_{1/e}}$) was determined where 63.2% of $\boldsymbol{E_{TOS}}$ (or $\boldsymbol{E_{TON}}$) was dry deposited, i.e., $\sum_{d=0}^{d_{1/e}} \boldsymbol{D}(\boldsymbol{d}) = 0.368\boldsymbol{E_{TOS}}$. The atmospheric lifetimes ($\boldsymbol{\tau}$) were derived as $\boldsymbol{\tau} = \boldsymbol{d_{1/e}}/\boldsymbol{u}$, where $\boldsymbol{u}$ was the average wind speed across

Formatted: Superscript

412 the distance $d_{1/e}$. These estimates were compared with predictions from the regional air quality
413 model GEM-MACH (Makar et al., 2018; Moran et al., 2010; SI Section S5) using facility
414 emission rates (Table 2). For **TOS** during F19, (Figure 3b, e), the observed cumulative
415 deposition at the maximum distance accounted for 74±5% vs. the modelled 21% of E_{TOS}. ~~,~~The
416 measurements indicate that the cumulative deposition of TOS was due mostly to SO_2 dry
417 deposition ~~(>92%).~~where ~~-~~ SO_2 was ~100% of TOS closest to the oil sands sources decreasing to
418 94% farthest downwind. Although the modelled cumulative deposition of TOS was significantly
419 lower than the observations, the fractional deposition of SO_2 was similar, decreasing from
420 ~100% to 95% of TOS. Fitting a curve to D and interpolating the cumulative deposition fraction
421 to the 63.2% E_{TOS} loss leads to a $d_{1/e}$ of 71±1 km, versus 500 km for the model prediction.
422 Under the prevailing wind conditions, the observed distance indicates a τ for **TOS** of
423 approximately 2.2 hours, whereas the model prediction indicated 16 hours. Large observation-
424 based values and model prediction differences in lifetime were also evident for the other flights
425 (SI Table S1). Clearly, the model predictions significantly underestimated deposition and vastly
426 overestimated $d_{1/e}$ and τ. The observation-based values for τ are also lower than average
427 lifetimes of 1–2 days for SO_2 and 2–9 days for pSO_4 derived from global models (Chin et al.,
428 2000; Benkovitz et al., 2004; Berglen et al., 2004), which include the effects of wet deposition
429 and chemical conversion for SO_2, thus making their implicit residence times with respect to dry
430 deposition even longer.
431 For **TON** in F19 (Figure 3h, l), the observed cumulative deposition accounted for
432 49±11% of E_{TON} at the maximum flight distance, versus 19% predicted by the model. Similar
433 model underestimates for cumulative deposition fractions were found for F7 and F20.
434 Extrapolating to the 63.2% cumulative deposition fraction, $d_{1/e}$ was estimated to be 190±7 km for

Formatted: Subscript

Formatted: Subscript

F19 versus a predicted 650 km from the model, implying a $\boldsymbol{\tau}$ of approximately 5.6 hours for the measurement-based results and 23 hours for the model prediction. Again, analogous differences for F7 and F20 were found (SI Table S1). Similar to TOS, the measurement-based $\boldsymbol{d_{1/e}}$ and $\boldsymbol{\tau}$ values for TON were significantly smaller than commonly accepted lifetimes of a few days for nitrogen oxides in the boundary layer (Munger et al., 1998).

3.3 Dry Deposition Fluxes *F*

Using the deposition rate ***D*** (in tonnes S or N hr^{-1})~~,~~, the average dry deposition fluxes, ***F*** (in tonnes S or N km^{-2} hr^{-1}), were calculated by dividing ***D*** by the plume footprint surface areas estimated by extending to the plume edges where the concentrations fell to background levels (Methods, Section 2.4). These footprints are shown as the gray shaded geographic areas in Figure 1, totaling 3500, 5700 and 4200km^2 for F7, F19, and F20 plumes, respectively; see SI Table S1 for **TON** plume areas). Figure 4a shows $\boldsymbol{F_{TOS}}$ values for all three flights, exhibiting exponential decreases with increasing distance away from the sources and showing e-folding distances for $\boldsymbol{F_{TOS}}$ of 18, 27, and 55 km for F7, F19, and F20, respectively. More than 90% of the decreases in $\boldsymbol{F_{TOS}}$ were accounted for by $\boldsymbol{F_{SO2}}$. Similarly, $\boldsymbol{F_{TON}}$ decreased exponentially with increasing transport distances in all flights (Figure 4c), exhibiting e-folding distances of 18 and 33 km for F7 and F19, and 55 and 189 km for the south and north **TON** plumes during F20, respectively. These e-folding distances were similar to those for $\boldsymbol{F_{TOS}}$, indicating similar rates of decreases in $\boldsymbol{F_{TON}}$ with transport distances.

The potential for other processes to contribute to the derived TOS and TON fluxes were considered including losses from the boundary layer to the free troposphere and re-emission of TOS or TON species from the surface back to the gas-phase. Two different approaches, a finite jump model and a gradient flux approach (Stull, 1988; Degrazia et al., 2015), were used to

Formatted: Superscript

Formatted: Superscript

Formatted: Not Highlight

estimate the potential upward loss across the interface between the boundary layer and the free troposphere for sulfur and nitrogen. In both approaches, the upward S flux was a minor loss at < 45 g km^{-2} hr^{-1}, about 3 orders of magnitude lower than the several to many kg km^{-2} hr^{-1} horizontal advectional transport that were determined using TERRA. For N, the upward flux was estimated to be ~570 g km^{-2} hr^{-1}, so although a larger flux than S, it is about factor of 18 lower than the TON fluxes derived from observations.

As expected from the $\boldsymbol{\tau}$ and transport e-folding distance $\boldsymbol{d_{1/e}}$ comparisons, the GEM-MACH model $\boldsymbol{F_{TOS}}$ were significantly lower than the measurement-based $\boldsymbol{F_{TOS}}$ results (Figure 4a), with the model $\boldsymbol{F_{TOS}}$ e-folding distances usually large: 133, 797, and 57 km for F7, F19, and F20, respectively, or 7.4, 29.5, and 1.1 times longer than the corresponding measurement results. Part of the differences between model and measurement $\boldsymbol{F_{TOS}}$ could be explained by differences in actual versus model emissions, $\boldsymbol{E_{TOS}}$ (Tables 1 vs 2). To remove the influence of emissions, an emission-normalized flux (=$\boldsymbol{F_{TOS}}/\boldsymbol{E_{TOS}}$ and $\boldsymbol{F_{TON}}/\boldsymbol{E_{TON}}$) was calculated for both measurement and model (SI Figure S2~~1~~). Figure 4b shows the ratios of measurement to model normalized emissions for TOS. The model emission-normalized fluxes $\boldsymbol{F_{TOS}}/\boldsymbol{E_{TOS}}$ were lower than the measurement-based values by factors of 2.5-14, 1.8-3.4, and 2.0-3.0 for F7, F19, and F20, respectively, decreasing with increased transport distances. However, they coalesce to a factor of 2 at the furthest distances sampled by the aircraft, indicating that the model $\boldsymbol{F_{TOS}}$ estimates were biased low by similar factors. The decreasing trends suggest that at distances further downwind, model fluxes may exceed measurement-based fluxes, albeit at magnitudes lower than those shown in Figure 4a, which is consistent with earlier study results (Makar et al., 2018). For $\boldsymbol{F_{TON}}$, the model-predicted values were also lower than the measurement results, especially near the sources (Figure 4c), and showed little variation with transport distances from the oil sands

sources for all flights, in strong contrast to the exponential decays observed from the aircraft. However, the emission-normalized fluxes (=$\boldsymbol{F_{TON}/E_{TON}}$) for the model approached those from measurements within maximum flying distances for F19 and F20, although still significantly lower for F7 (>10x) (Figure 4d).

3.4 Dry Deposition Velocities V_d

The shorter $\boldsymbol{d_{1/e}}$ and $\boldsymbol{\tau}$, and larger deposition fluxes $\boldsymbol{F}$ near the sources determined from the aircraft measurements compared to predictions by the GEM-MACH model indicate that the model dry deposition velocities $\boldsymbol{V_d}$ was underestimated. Gas-phase $\boldsymbol{V_d}$ in the model is predicted with a standard inferential "resistance" algorithm (Wesley, 1989; Jarvis, 1976), with resistance to deposition calculated for multiple parameters including aerodynamic, quasi-laminar sublayer and bulk surface resistances (Baldocchi, 1987). To demonstrate the model underestimation in $\boldsymbol{V_d}$, comparisons between the measurement-based and model $\boldsymbol{V_d}$ were made where an evaluation of $\boldsymbol{V_d}$ for **TOS** and **TON** was possible. All $\boldsymbol{F_{SO2}}$ were converted into $\boldsymbol{V_{d\text{-}SO2}}$ by dividing $\boldsymbol{F_{SO2}}$ by interpolated SO_2 concentrations at 40 meters above ground, averaging 1.2±0.5, 2.4±0.4, and 3.4±0.6 cm s^{-1} for F7, F19 and F20, respectively, across the plume footprints (Methods, Section 2.4 and SI Table S2). The corresponding model $\boldsymbol{V_{d\text{-}SO2}}$ derived in the same way as the observations was 0.72, 0.63, and 0.58 cm s^{-1}, 1.7-5.4 times lower than observations (SI Section S5; SI Table S2). Interestingly, the median $\boldsymbol{V_d}$ for SO_2 of 4.1 cm s^{-1} determined using eddy covariance/vertical gradient measurements from a tower in the AOSR is higher than the mass balanced method showing an even larger discrepancy compared to the model (SI Section S3; Figure S5~~4~~). Similarly, derived $\boldsymbol{V_{d\text{-}TON}}$ averaged 2.8±0.8, 1.6±0.5, 4.7±1.4 and 2.2±0.7 cm s^{-1} F7, F19, F20 south plume, and F20 north plume, respectively (SI Table S2), 1.2-5.2 times higher than the corresponding modelled $\boldsymbol{V_{d\text{-}TON}}$ of 1.4, 1.3, 0.92, and 0.90 cm s^{-1}.

Using the observations, it was not possible to derive individual TON deposition rates separate from their chemical formation/losses. In previous modelling work, Makar et al. (2018), use the GEM-MACH model and describe the relative contributions of different TOS and TON species towards total S and N deposition in the AOSR. TON was dominated by dry NO_2 (g) deposition fluxes close to the sources (>70% of total N close to the sources), and dry HNO_3 (g) deposition increases with increasing distance from the sources (remaining < 30% of total N), and other sources of TON having minor contributions to deposition (< 10%). Although TON encompasses a range of different N species with expected differences in their deposition rates, comparisons of $V_{d\text{-}TON}$ with the model show, nevertheless, that overall large differences do exist.

Formatted: Font: 12 pt

Formatted: Not Highlight

3.5 Monte-Carlo simulations of V_d for SO_2

To further demonstrate observation-model differences, $\boldsymbol{V_d}$ distributions of SO_2 from five common inferential dry deposition algorithms (Wu et al., 2018; Makar et al., 2018) were determined for the conditions encountered during the flights using a Monte-Carlo approach as described in Methods, Section 2.5). Results for the $\boldsymbol{V_d}$ simulations algorithms are shown in Figure 5a. Histograms for all five algorithms have peak $\boldsymbol{V_d}$ values at ~1 cm s^{-1} or lower. Probability distributions for the individual resistance terms, R_a, R_b, and R_c showed that the dominant resistance driving $\boldsymbol{V_d}$ was the R_c term (SI Figure S3~~2~~). Also shown in Figure 5a are the measurement-derived $\boldsymbol{V_d}$ for Flights 7, 19 and 20, and that from the Oski-ôtin ground site. The observed $\boldsymbol{V_d}$ values are larger than the $\boldsymbol{V_d}$ values for most of the simulations, with the exception of Flight 7, where the Zhang et al. (2002), NOAH-GEM (Wu et al., 2018) and C5DRY (Wu et al., 2018) algorithms' distributions agree with the observations. All algorithms are biased low

relative to the observations for the remaining flights, and the Oski-ôtin ground site. It is noted that the ground-site observations that were derived using a standard flux tower methodology (SI Section S3) at a single site, appeared to be higher than all other $\boldsymbol{V_d}$; nevertheless, these observations are closer to the aircraft values than the algorithm estimates. These results indicate that an underestimation of $\boldsymbol{V_d}$ relative to both aircraft and ground based measurements in the AOSR ~~region~~ is not unique to the GEM-MACH model or its dry deposition algorithm; similar results would occur with the other algorithms included in the Monte-Carlo simulations, all of which are used within other regional models.

To investigate the possible reasons behind the low model $\boldsymbol{V_d}$ relative to the observations, a series of sensitivity tests using SO_2 were conducted. Differences in model $\boldsymbol{V_d}$ have been shown to be mainly due to differences in the calculated R_c (Wu et al., 2018), and sensitivity tests here indicated that R_c is particularly sensitive to the cuticular resistance R_{cut}. Hence, factors causing R_{cut} to change can have significant impact on model $\boldsymbol{V_d}$. In some of the algorithms, R_{cut} and other resistance terms are dependent on the effective Henry's Law constant K_H^* for SO_2. The Monte-Carlo simulations for Figure 5 assumed a surface pH= 6.68 resulting in a K_H^* of $1x10^5$ for SO_2. Additional Monte-Carlo simulations were performed for the GEM-MACH dry deposition algorithm by adjusting K_H^* assuming different pH with small variations from a pH=6.68 significantly changing R_c, R_{cut}, and $\boldsymbol{V_d}$ (SI Figure S~~43~~). In Figure 5b – red dashed line, with a surface pH change from 6.68 to 8, consistent with possible alkaline surfaces in the AOSR (Makar et al., 2018), in the GEM-MACH simulation, the $\boldsymbol{V_d}$ distribution is moved to larger values) with its peak value shifting from 0.6 to 1.4 cm s^{-1}. These results show that model $\boldsymbol{V_d}$ may be highly sensitive to assumed surface pH, at least when using some inferential dry deposition algorithms which are pH-dependent. However, Figure 5b shows that this pH-associated increase

in V_d is still insufficient to encompass the range of measurement-derived V_d. Increasing pH to 8 for the GEM-MACH simulation reduces R_{cut}, hence R_c, to values much smaller than R_a and R_b, suggesting that model V_d cannot further increase without reductions in both R_a and R_b. In other words, R_a and R_b were probably overestimated in the current deposition velocity algorithms. By using the Zhang et al. (2002) R_a and the NOAH-GEM (Wu et al., 2018) R_b parameterizations in the GEM-MACH algorithm, a further shift of the GEM-MACH V_d distribution to larger values was found, with the range encompassing most of the observations (Figure 5b, pink dashed line).

The potential for re-emission of TOS and TON species was also considered. Fulgham et al. (2020) report that the bidirectional fluxes of volatile organic acids are driven by an equilibrium partitioning between surface wetness and the atmosphere. The observations presented here represent the net flux of all processes including the effects of deposition and any potential re-emissions of TOS and TON compounds should this process occur. As the results show a net downward flux (i.e. net deposition), if any re-emission was occuring, it would be smaller than the deposition fluxes observed here, which are themselves higher than shown by currently available deposition algorithms. This implies that the deposition part of the flux must be even larger than the net observed flux and the measured net fluxes presented here should then be considered as minimum values. The current deposition algorithms do not include bidirectional fluxes for inorganics, and adjustments related to pH in some situations may not be sufficient to parameterize deposition fluxes. A bidirectional approach may be needed that would include not only $[H^+]$, but surface heterogeneous reactions, to determine near-surface equilibrium concentrations of co-depositing gases such as ammonia and nitric acid.

It is c~~C~~lear~~ly,~~ from the Monte-Carlo simulations for SO_2 V_d comparisons, inferential dry deposition algorithms as used in regional and global chemical transport models need to be further

Formatted: Font: 12 pt, Not Highlight

Formatted: Font: 12 pt

Formatted: Font: 12 pt, Not Highlight

Formatted: Font: 12 pt

Formatted: Font: 12 pt, Not Highlight

Formatted: Font: 12 pt

validated and improved, especially over large geographic regions. Here, the role of pH was identified for improvement in some algorithms along with possible improvement in aerodynamic and quasi-laminar sublayer resistance parameters. Yet, for other algorithms and for **TON** compounds, the model low-biases in V_d remain to be investigated.

The underestimates suggest that the applications of these algorithms in regional or global models may significantly underestimate ~~model~~ predictions of **TOS** dry depositional loss from the atmosphere. Underestimates in V_d are the result of a combination of uncertainties in the parameterizations of each algorithm. In the case of the algorithm used in GEM-MACH, by adjusting the assumed surface pH from 6.68 to 8 (justifiable given the considerable dust emissions in the region (Zhang et al., 2018)), the model V_d moved closer to the aircraft-derived values (Figure 5b), reducing the model-observation gap by approximately 2/3. In addition, substituting the aerodynamic resistance and quasi-laminar sublayer resistance parameterizations in the GEM-MACH algorithm with that from Zhang et al. (2002) and NOAH-GEM (Wu et al., 2018), respectively, resulted in a further increase in the model V_d distribution that encompasses most of the observations (Figure 5b). Clearly, different algorithms respond differently to changes in the parameterizations, and validation and adjustment to each algorithm needs measurement-based results over large regions such as derived here.

4 Conclusions

The atmospheric transport distances and lifetimes $d_{1/e}$ and τ determined from the aircraft measurements are substantially shorter than the GEM-MACH model predictions, and the dry deposition fluxes F and velocities ~~F~~ and V_d near sources are larger compared to the predictions by GEM-MACH and five inferential dry deposition velocity algorithms, respectively. There are

Formatted: Font: Bold, Italic

596 important implications for these measurement-model discrepancies. Such discrepancies indicate
597 that regional or global chemical transport models using these algorithms are biased low for local
598 deposition and high for long-range transport and deposition, and **TOS** and **TON** loss from the
599 atmosphere are significantly under-predicted, resulting in overestimated lifetimes. While the
600 measurements took place over a relatively short time period, these results indicate that TOS and
601 TON may be removed from the atmosphere at about twice the rate as predicted by current
602 atmospheric deposition algorithms. This, in turn, implies a potentially significant impact on
603 deposition over longer time scales (potentially weeks to months) and relevance towards
604 cumulative environmental exposure metrics such as critical loads and their exceedance. A faster
605 near-source deposition velocity for emitted reactive gases may imply less S and N mass being
606 available for long range transport, reducing concentrations and deposition further downwind.
607 The near-source higher deposition velocity, thus has the important implication of a reduction in
608 more distant and longer timescale deposition for locations further from the sources. Moreover,
609 emissions assessed through network measurements or budget analysis of atmospheric **TOS** and
610 **TON** (Sickles and Shadwick, 2015; Paulot et al., 2018; Berglen et al., 2004) may be
611 underestimated due to lower $\boldsymbol{V_d}$ used in these estimates, and may require reassessing the
612 effectiveness of control policies. Shorter $\boldsymbol{\tau}$ for **TOS** and **TON** reduces their atmospheric spatial
613 scale and intensity of smog episodes, potentially reducing human exposures (Moran et al., 2010).
614 Importantly, shorter $\boldsymbol{\tau}$ for **TOS** and **TON** reduces their contribution to atmospheric aerosols;
615 consequently, the negative direct and indirect radiative forcing from these sulfur and nitrogen
616 aerosols are reduced, reducing their cooling effects on climate (Solomon et al., 2007). These
617 impacts suggest that more measurements to determine $\boldsymbol{\tau}$ and $\boldsymbol{F}$ for these pollutants across large
618 geographic scales and different surface types are necessary to better quantify their climate and

environmental impacts in support of policy. While in the past such determination was difficult and/or impossible, the present study provides a viable methodology to achieve such a goal.

Table 1. Average observed meteorological conditions and facility emission rates of **TOS** (E_{TOS}) and **TON** (E_{TON}), (determined from extrapolated (to distance=0) transfer rates; Figure 1) for **TOS** and **TON** during the F7, F19 and F20 flights. SP=south plume; NP=north plume.

Flight	Date	Time (UTC)	Mean wind speed (m/s)	Mean wind direction (°)	Mixed layer height (m agl)	E_{TOS} (t/hr)	E_{TON} (t/hr)
7	Aug 19/13	2007–0108	13.0±1.0	256±11.7	2500±100	3.4	1.2
19	Sep 4/13	1854–2353	9.5±1.9	218±16	1200±100	18.5	3.9
20	Sep 5/13	1933-2436	8.9±1.2	281±11	2100±100	5.8	2.2 (SP) 1.2 (NP)

Table 2. Model average meteorological conditions and facility emission rates of **TOS** (E_{TOS}) and **TON** (E_{TON}) during the F7, F19 and F20 flights as described above. SP=south plume; NP=north plume.

Flight	Date	Time (UTC)	mean wind speed (m/s)	mean wind direction (°)	mixed layer height (m agl)	E_{TOS} (t/hr)	E_{TON} (t/hr)
7	Aug 19/13	2007–0108	12.6±0.3	253±5.0	1670±80	3.8	2.9
19	Sep 4/13	1854–2353	8.1±1.0	225±4.6	1450±43	4.3	2.4
20	Sep 5/13	1933-2436	9.1±0.7	275±1.6	1590±42	3.7	1.5 (SP) 0.9 (NP)

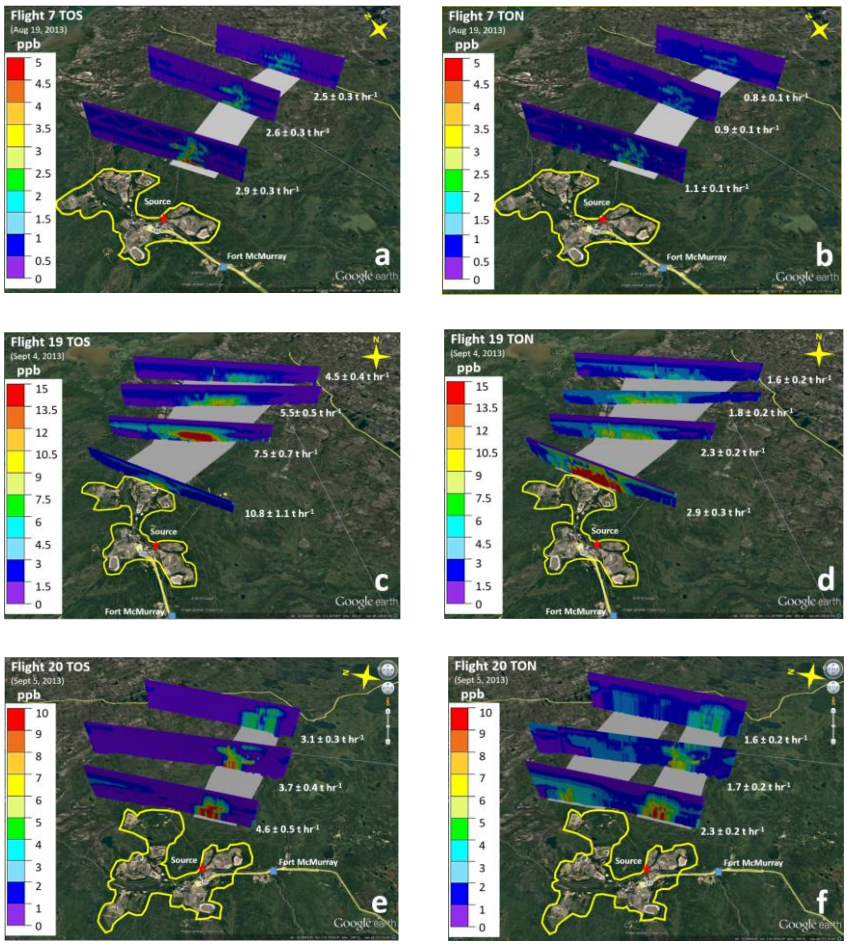

Figure 1. **TOS** (total oxidized sulfur) and **TON** (total oxidized nitrogen) plumes downwind of the AOSR during three Lagrangian flights, F7, F19 and F20. The AOSR facilities are enclosed by the yellow outline. The transfer rates ***T*** in t S or N hr^{-1} across each screen are shown. The grey shaded surface areas are identified as the geographic footprint under the plumes. Data: Google Image © 2018 Image Landsat / Copernicus.

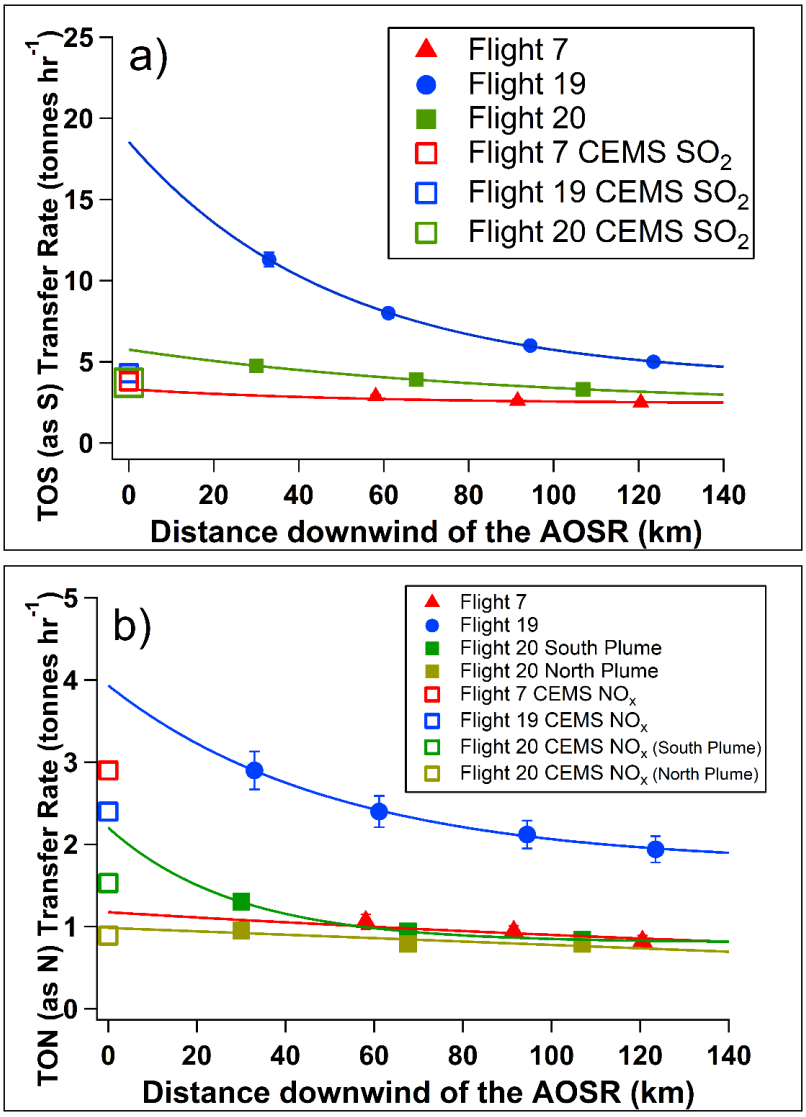

638

639 **Figure 2**. TERRA-derived transfer rates of (a) **TOS** and (b) **TON** for F7, F19 and F20. The
640 vertical bars indicate the propagated uncertainties. The model emission rates E_{TOS} and E_{TON} are
641 shown by the open symbols.

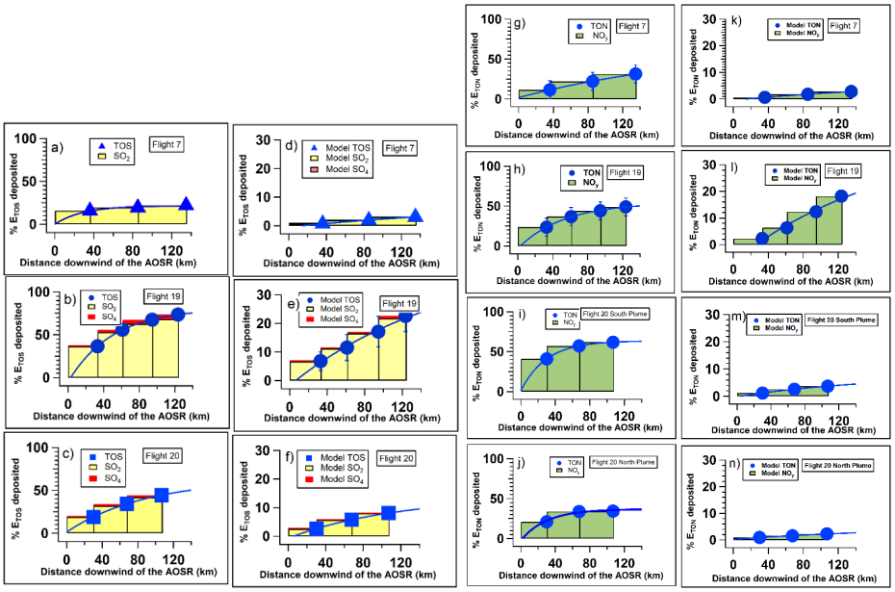

642

643 **Figure 3**. Cumulative dry deposition as a percentage of emissions ~~of~~ E_{TOS} (a to f) or E_{TON} (g to
644 n) for F7, F19 and F20 measurements ~~and~~ with corresponding GEM-MACH model predictions.
645 The bars show the dry deposition due to SO_2 and pSO_4. The curves were fitted to the **TOS** and
646 **TON** dry deposition percentages from which $d_{1/e}$ and τ were determined.

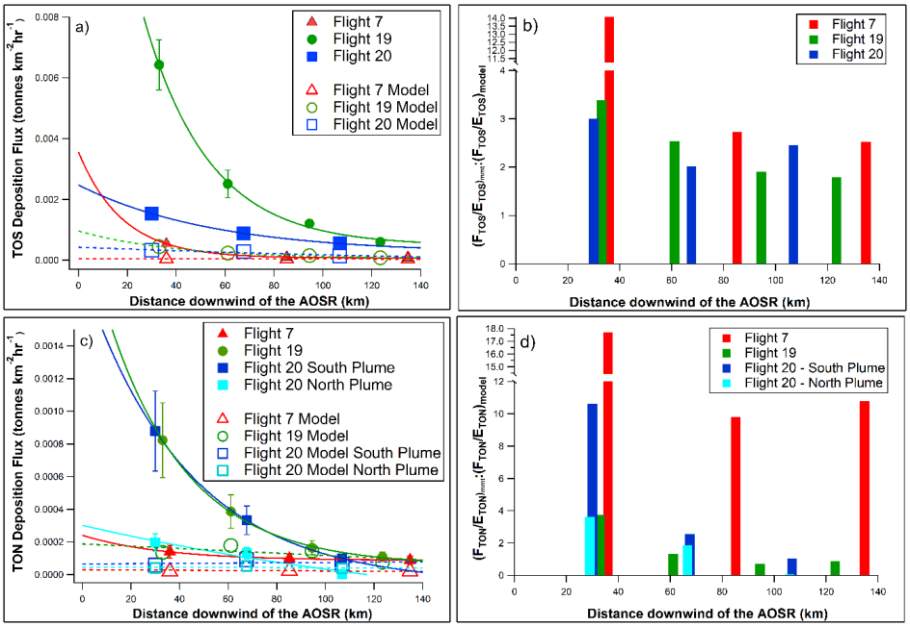

Figure 4. Dry deposition fluxes F_{TOS} and F_{TON} (in t km^{-2} hr^{-1}) determined from measurements (solid symbols) and GEM-MACH model predictions (open symbols). (a) F_{TOS}, (b) ratios of measurement to model normalized emissions F_{TOS}/E_{TOS}, (c) F_{TON}, and (d) ratios of measurement to model normalized emissions F_{TON}/E_{TON}.

Formatted: Superscript

Formatted: Superscript

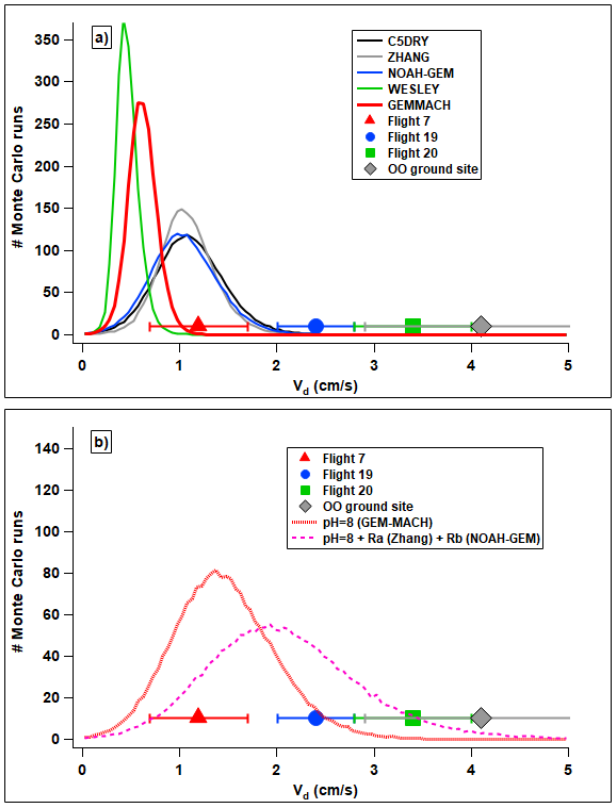

Figure 5. (a) Distributions of V_d for SO_2 from Monte-Carlo simulations using 5 different deposition parameterizations (Wu et al., 2018; Makar et al., 2018) and (b) Monte-Carlo simulations for the GEM-MACH algorithm using a pH=8 and using a pH=8 plus replacing the GEM-MACH algorithm R_a and R_b formulae with that from Zhang et al. (2002) and NOAH-GEM (Wu et al., 2018), respectively. Aircraft-derived V_d for F7, F19 and F20 as well as the median value for the Oski-ôtin ground site (SI Figure S54) are shown in both (a) and (b) for comparison.

References

Aubinet, M., Vesala, T. and Papale, D. (Eds.): Eddy Covariance. Springer Atmospheric Sciences, Springer, Dordrecht, 2012.

Baldocchi, D.D., Vogel, C.A., and Hall, B.: A canopy stomatal resistance model for gaseous deposition to vegetated surfaces, Atmos. Env., **21**, 91-101, https://doi.org/10.1016/0004-6981(87)90274-5, 1987.

Baray, S., Darlington, A., Gordon, M., Hayden, K.L., Leithead, A., Li, S.-M., Liu, P.S.K., Mittermeier, R.L., Moussa, S.G., O'Brien, J., Staebler, R., Wolde, M., Worthy, D. and McLaren, R.: Quantification of methane sources in the Athabasca Oil Sands Region of Alberta by aircraft mass balance, Atmos. Chem. Phys., **18**, 7361-7378, https://doi.org/10.5194/acp-18-7361-20182018.

Benkovitz, C.M., Schwartz, S.E., Jensen, M.P., Miller, M.A., Easter, R.C. and Bates, T.S.: Modeling atmospheric sulfur over the Northern Hemisphere during the Aerosol Characterization Experiment 2 experimental period, J. Geophys. Res., **109**, D2220, https://doi.org/10.1029/2004JD004939, 7, 2004.

Berglen, T.F., Berntsen, T.K., Isaksen, I.S.A. and Sundet, J.K.: A global model of the coupled sulfur/oxidant chemistry in the troposphere: The sulfur cycle, J. Geophys. Res., **109**, D19310, https://doi.org/10.1029/2003JD003948, 2004.

Bobbink, R., Hicks, K., Galloway, J., Spranger, T., Alkemade, R., Ashmore, M., Bustamante, M., Cinderby, S., Davidson, E., Dentener, F., Emmett, B., Erisman, J-W., Fenn, M., Gilliam, F., Nordin, A., Pardo, L. and De Vries, W.: Global assessment of nitrogen deposition effects on terrestrial plant diversity: a synthesis, Ecol. Appl. **20**, 30-59, https://doi.org/10.1890/08-1140.1, 2010.

Brook, J.R., Di-Giovanni, F., Cakmak, S. and Meyers, T.P.: Estimation of dry deposition velocity using inferential models and site-specific meteorology – uncertainty due to siting of meteorological towers, Atmos. Environ., **31**, 3911-3919, https://doi.org/10.1016/S1352-2310(97)00247-1, 1997.

Chin, M., Savoie, D.L., Huebert, J., Bandy, A.R., Thornton, D.C., Bates, T.S., Quinn, P.K., Saltzman, E.S. and De Bruyn, W.J.: Atmospheric sulfur cycle simulated in the global model GOCART: Comparison with field observations and regional budgets, J. Geophys. Res., **105**, 24689-24712, https://doi.org/10.1029/2000JD900384, 2000.

Christian, G., Ammann, M., D'Anna, B., Donaldson, D.J. and Nizkorodov, S.A.: Heterogeneous photochemistry in the atmosphere, Chem. Rev. **115**, 4218-4258, https://doi.org/10.1021/cr500648z, 2015.

DeCarlo, P.F. , Kimmel, J.R., Trimborn, A., Northway, M.J., Jayne, J.T., Aiken, A.C., Gonin, M., Fuhrer, K., Horvath, T., Docherty, K.S., Worsnop, D.R., Jimenez, J.L.: Field-deployable, high-resolution, time-of-flight aerosol mass spectrometer, Anal. Chem., 8281-9289, https://doi.org/10.1021/ac061249n, 2006.

de Gouw, J. and Warneke, C.: Measurements of volatile organic compounds in the earth's atmosphere using proton-transfer-reaction mass spectrometry, Mass Spectrom. Rev., 26, 223-257, https://doi.org/10.1002/mas.20119, 2007.

Degrazia, G.A., Maldaner, S., Buske, D., Rizza, U., Buligon, L., Cardoso, V., Roberti, D.R., Acevedo, O., Rolim, S.B.A. and Stefanello, M.B.: Eddy diffusivities for the convective boundary layer derived from LES spectral data, Atmos. Pollut. Res., **6**, 605-611, https://doi.org/10.5094/APR.2015.068, 2015.

Dentener, F., Drevet, J., Lamarque, J.F., Bey, I., Eickhout, B., Fiore, A.M., Hauglustaine, D., Horowitz, L.W., Krol, M., Kulshrestha, U.C., Lawrence, M., Galy-Lacaux, C., Rast, S., Shindell, D., Stevenson, D., Van Noije, T., Atherton, C., Bell, N., Bergman, D., Butler, T., Cofala, J., Collins, B., Doherty, R., Ellingsen, K., Galloway, J., Gauss, M., Montanaro, V., Müller, J.F., Pitari, G., Rodriguez, J., Sanderson, M., Solmon, F., Strahan, S., Schultz, M., Sudo, K., Szopa, S. and Wild, O.: Nitrogen and sulfur deposition on regional and global scales: A multimodel evaluation, Global Biogeochem. Cycle, **20**, GB4003, https://doi.org/10.1029/2005GB002672, 2006.

Doney, S.C. The growing human footprint on coastal and open-ocean biogeochemistry, Science **328**, 1512-1516, DOI: 10.1126/science.1185198, 2010.

Dunlea, E.J. Herndon, S.C., Nelson, D.D., Volkamer, R.M., San Martini, F., Sheehy, P.M., Zahniser, M.S. Shorter, J. H., Wormhoudt, J. C., Lamb, B. K., Allwine, E. J., Gaffney, J. S., Marley, N. A., Grutter, M., Marquez, C., Blanco, S., Cardenas, B., Retama, A., Ramos Villegas, C. R., Kolb, C. E., Molina, L. T., and Molina, M. J.: Evaluation of nitrogen dioxide chemiluminescence monitors in a polluted urban environment, Atmos. Chem. Phys., 7, 2691–2704, https://doi.org/10.5194/acp-7-2691-2007, 2007.

Emerson, E.W., Hodshire, A.L., DeBolt, H.M., Bilsback, K.R., Pierce, J.R., McMeeking, G.R., and Farmer, D.K., Revisiting particle dry deposition and its role in radiative effect estimates, Proc. Natl. Acad. Sci. U.S.A., 117 (42), 26076-26082, doi: 10.1073/pnas.2014761117, 2020.

Finkelstein, P.L., Ellestad, T.G., Clarke, J.F., Meyers, T.P., Schwede, D.B., Hebert E.O. and Neal, J.A.: Ozone and sulfur dioxide dry deposition to forests: Observations and model evaluation, J. Geophys. Res., **105**, 15365-15377, https://doi.org/10.1029/2000JD900185, 2000.

Fowler, D., Pilegaard, K., Sutton, M.A., Ambus, P., Raivonen, M., Duyzer, J., Simpson, D., Fagerli, H., Fuzzi, S., Schjoerring, J.K., Granier, C., Neftel, A., Isaksen, I.S.A., Laj, P., Maione, M., Monks, P.S., Burkhardt, J., Daemmgen, U., Neirynck, J., Personne, E., Wichink-Kruit, R., Butterbach-Bahl, K., Flechard, C., Tuovinen, J.P., Coyle, M., Gerosa, G., Loubet, B., Altimir, N., Gruenhage, L., Ammann, C., Cieslik, S. Paoletti, E., Mikkelsen, T.N., Ro-Poulsen, H., Cellier, P., Cape, J.N., Horváth, L., Loreto, F., Niinemets, Ü., Palmer, P.I., Rinne, J., Misztal, P., Nemitz, E., Nilsoon, D., Pryor, S., Gallagher, M.W., Vesala, T., Skiba, U., Bruggemann, N. Zechmeister-Boltenstern, S., Williams, J., O'Dowd, Facchini, M.C., de Leeuw, G., Flossman, A., Chaumerliac, N. and Erisman, J.W.: Atmospheric composition change: ecosystems-atmosphere interactions, Atmos. Environ., **43**, https://doi.org/10.1016/j.atmosenv.2009.07.068, 5193-5267, 2009.

Formatted: Font: (Default) Times New Roman

Formatted: Font: (Default) Times New Roman

Formatted: Font: (Default) Times New Roman

Formatted: Font: (Default) Times New Roman

Formatted: Font: (Default) Times New Roman

Formatted: English (Canada)

Formatted: English (Canada)

740 Fulgham, S.R., Millet, D.B., Alwe, H.D., Goldstein, A.H., Schobesberger, S., and Farmer, D.K.,
741 Surface wetness as an unexpected control on forest exchange of volatile organic acids,
742 Geophys. Res. Lett., 47, e2020GL088745, https://doi.org/10.1029/2020GL088745, 2020.

743 Gordon, M., Li, S.-M., Stabler, R., Darlington, A., Hayden, K., O'Brien, J. and Wolde, M.:
744 Determining air pollutant emission rates based on mass balance using airborne measurement
745 data over the Alberta oil sands operations, Atmos. Meas. Tech., **8**, 3745-3765,
746 https://doi.org/10.5194/amt-8-3745-2015, 2015.

747 Howarth, R.W. Review: coastal nitrogen pollution: a review of sources and trends globally and
748 regionally, Harmful Algae, **8**, 14-20, https://doi.org/10.1016/j.hal.2008.08.015, 2008.

749 Jarvis, P.G. The interpretation of the variations in leaf water potential and stomatal conductance
750 found in canopies in the field, Phil. Trans. R. Soc. Lond., B., **273**, 593-610,
751 https://doi.org/10.1098/rstb.1976.0035, 1976.

752 Li, S.-M., Leithead, A., Moussa, S.G., Liggio, J., Moran, M.D., Wang, D., Hayden, K.,
753 Darlington, A., Gordon, M., Staebler, R., Makar, P.A., Stroud, C.A., McLaren, R., Liu,
754 P.S.K., O'Brien, J., Mittermeier, R.L., Zhang, J., Marson, G., Cober, S.G., Wolde, M. and
755 Wentzell, J.J.B.: Differences between measured and reported volatile organic compound
756 emissions from oil sands facilities in Alberta, Canada, Proc. Natl. Acad. Sci., **114**, E3756-
757 E3765, https://doi.org/10.1073/pnas.1617862114, 2017.

758 Liggio, J., Li, S.-M., Hayden, K., Taha, Y.M., Stroud, C., Darlington, A., Drollette, B.D.,
759 Gordon, M. Lee, P., Liu, P., Leithead, A., Moussa, S.G., Wang, D., O'Brien, J., Mittermeier,
760 R.L., Brook, J.R., Lu, G., Staebler, R., Han, Yuemei, Tokarek, T.W., Osthoff, H.D., Makar,
761 P.A., Zhang, J., Plata, D.L. and Gentner, D.R.: Oil sands operations as a large source of
762 secondary organic aerosols, Nature, **534**, 91-94, https://doi.org/10.1038/nature17646, 2016.

763 Liggio, J., Li, S.-M., Staebler, R., Hayden, K., Darlington, A., Mittermeier, R.L., O'Brien, J.,
764 McLaren, R., Wolde, M. Worthy, D. and Vogel, F.: Measured Canadian oil sands CO2
765 emissions are higher than estimates made using internationally recommended methods,
766 Nature Comm., **10**, 1863, https://doi.org/10.1038/s41467-019-09714-9, 2019.

767 Makar, P.A., Akingunola, A., Aherne, J., Cole, A.S., Aklilu, Y., Zhang, J., Wong, I., Hayden, K.,
768 Li, S.-M., Kirk, J., Scott, K., Moran, M.D., Robichaud, A., Cathcart, H., Baratzedah, P.,
769 Pabla, B., Cheung, P., Zheng, Q. and Jeffries, D.S.: Estimates of exceedances of critical loads
770 for acidifying deposition in Alberta and Saskatchewan, Atmos. Chem. Phys., **18**, 9897-9927,
771 https://doi.org/10.5194/acp-18-9897-2018, 2018.

772 Matsuda, K., Watanabe, I., Wingpud, V. and Theramongkol, P.: Deposition velocity of O_3 and
773 SO_2 in the dry and wet season above a tropical forest in northern Thailand, Atmos. Environ.,
774 **40**, 7557-7564, https://doi.org/10.1016/j.atmosenv.2006.07.003, 2006.

775 Meyers, T.P., Hicks, B.B., Hosker Jr, R.P., Womack, J.D. and Satterfield, L.C.: Dry deposition
776 inferential measurement techniques. II. Seasonal and annual deposition rates of sulfur and
777 nitrate, Atmos. Environ., **25**, 2631-2370, https://doi.org/10.1016/0960-1686(91)90110-S,
778 1991.

779 Moran, M.D., Ménard, S., Pavlovic, R., Anselmo, D., Antonopoulos, S., Makar, P.A., Gong, W.,
780 Gravel, S., Stroud, C., Zhang, J., Zheng, Q., Robichaud, A., Landry, H., Beaulieu, P.-A.,
781 Gilbert, S., Chen, J. and Kallaur, A.: Recent advances in Canada's national operational AQ
782 forecasting system. In: Steyn DG, Rao ST (Eds) Air Pollution Modelling and Its Application,
783 Springer, Dordrecht, 289,
784 https://www.researchgate.net/deref/http%3A%2F%2Fdx.doi.org%2F10.1007%2F978-94-007-
785 5577-2_37, 2010.

786 Munger, J.W., Fan, S., Bakwin, P.S., Goulden, M.L., Goldstein, A.H., Colman, A.S. and Wolfsy,
787 S.C.: Regional budgets for nitrogen oxides from continental sources: Variations of rates for
788 oxidation and deposition with season and distance from source regions, J. Geophys. Res., **103**,
789 8355-8368, https://doi.org/10.1029/98JD00168, 1998.

790 Paulot, F., Malyshev, S., Nguyen, T., Crounse, J.D., Shevliakova, E. and Horowitz, L.W.:
791 Representing sub-grid scale variations in nitrogen deposition associated with land use in a
792 global Earth system model: implications for present and future nitrogen deposition fluxes over
793 North America, Atmos. Chem. Phys. **18**, 17963-17978, https://doi.org/10.5194/acp-18-17963-
794 2018, 2018.

795 Samset, B.H., Myhre, G., Herber, A., Kondo, Y., Li, S.-M., Moteki, N., Koike, M., Oshima, N.,
796 Schwarz, J.P., Balkanski, Y., Bauer, S.E., Bellouin, N., Berntsen, T.K., Bian, H., Chin, M.,
797 Diehl, T., Easter, R.C., Ghan, S.J., Iversen, T., Kirkevåg, A., Lamarque, J.-F., Lin, G., Liu,
798 X., Penner, J.E., Schulz, M., Seland, Ø., Skeie, R.B., Stier, P., Takemura, T., Tsigaridis, K.
799 and Zhang, K.: Modelled black carbon radiative forcing and atmospheric lifetime in AeroCom
800 Phase II constrained by aircraft observations, Atmos. Chem. Phys. **14**, 12465–12477,
801 doi:10.5194/acp-14-12465-2014, 2014.

802 Sickles, J.E. & Shadwick, D.S. Air quality and atmospheric deposition in the eastern US: 20
803 years of change. Atmos. Chem. Phys., **15**, 173-197, https://doi.org/10.5194/acp-15-173-2015,
804 2015.
805
806 Solomon, S., Quin, M., Manning, Z., Chen, M. Marquis, K.B., Averyt, M., Tignor, M., and
807 Miller, H.L. (Eds): Climate Change 2007: The Physical Science Basis, IPCC *AR4*,
808 Cambridge University Press, 2007.

809 Stull, R. Introduction to Boundary Layer Meteorology, Kluwer Academic Press, 1988.

810 Vet, R., Artz, R.S., Carou, S., Shaw, M., Ro, C.-U., Aas, W., Baker, A., Bowersox, V.C.,
811 Dentener, F., Galy-Lacaux, C., Hou, A., Pienaar, J., Gillett, R., Forti, M.C., Gromov, S., Hara,
812 H., Khodzher, T., Mahowald, N.M., Nickovic, S., Rao, P.S.P. and Reid, N.W.: A global
813 assessment of precipitation chemistry and deposition of sulfur, nitrogen, sea salt, base cations,
814 organic acids, acidity and pH, and phosphorus, Atmos. Environ., **93**, 3-100,
815 https://doi.org/10.1016/j.atmosenv.2013.10.060, 2014.

816 Wesley, M.L. Parameterization of surface resistances to gaseous dry deposition in regional-scale
817 numerical models, Atmos. Environ., **23**, 1293-1304,
818 https://ui.adsabs.harvard.edu/link_gateway/1989AtmEn..23.1293W/doi:10.1016/0004-
819 6981(89)90153-4, 1989.

Field Code Changed

Wesley, M.L. & Hicks, B.B. A review of the current status of knowledge on dry deposition, Atmos. Environ., **34,** 2261-2282, https://ui.adsabs.harvard.edu/link_gateway/2000AtmEn..34.2261W/doi:10.1016/S1352-2310(99)00467-7, 2000.

WHO, Ambient Air Pollution: A Global Assessment of Exposure and Burden of Disease, 2016.

Williams, E.J., Baumann, K., Roberts, J.M., Bertman, S.B., Norton, R.B., Fehsenfeld, F.C., Springston, S.R., Nennermacker, L.J., Newman, L., Olszyna, K., Meagher, J., Hartsell, B., Edgerton, E., Pearson, J.R., and Rodgers, M.O., Intercomparisons of ground-based NOy measurement techniques, J. Geophys. Res., 103, 22,621-22,280, https://doi.org/10.1029/98JD00074,1998.

Wright, L.P., Zhang, L., Cheng, I. and Aherne, J.: Impacts and effects indicators of atmospheric deposition of major pollutants to various ecosystems - a review, Aerosol Air Quality Res., **18**, 1953-1992, https://doi.org/10.4209/aaqr.2018.03.0107, 2018.

Wu, Z., Schwede, D.B., Vet, R., Walker, J.T. Shaw, M. Staebler, R. and Zhang, L.: Evaluation and intercomparison of five North American dry deposition algorithms at a mixed forest site, J. Adv. Mod. Earth Sys., **10**, 1571-1586, https://doi.org/10.10292017MS001231, 2018.

Zhang, L., Moran, M.D., Makar, P., and Brook, J.R.: Modelling gaseous dry deposition in AURAMS: a unified regional air-quality modelling system, Atmos. Environ., **36**, 537-560, 2002.Zhang, J., Moran, M.D., Zheng, Q., Makar, P.A., Baratzadeh, P., Marson, G., Liu, P. and Li, S.-M.: Emissions preparation and analysis for multiscale air quality modeling over the Athabasca Oil Sands Region of Alberta, Canada, Atmos. Chem. Phys., **18**, 10459-10481, https://doi.org/10.5194/acp-18-10459-2018, 2018.

Author Contribution:

KH, SML, JL, SM, RM, RS, JO, MW all contributed to the collection of aircraft observations in the field. KH, RM and JO made the SO_2, NO_y and pSO_4 measurements and carried out subsequent QA/QC of data. RM analyzed canister VOCs and provided OH concentration estimates. SM provided OH estimates from MCM modelling as a comparison. AD contributed to the development of TERRA. JL wrote the Monte Carlo code. PM and AA ran the model and provided model analyses. JZ provided emissions data. LZ and RS provided deposition algorithm parameters. KH and SML wrote the paper input from all co-authors.

Code availability

All the computer code associated with the TERRA algorithm, including for the kriging of pollutant data, a demonstration dataset and associated documentation is freely available upon request. The authors request that future publications which make use of the TERRA algorithm cite this paper, Gordon et al., Liggio et al., or Li et al. as appropriate.

Formatted: Space After: 0 pt

Field Code Changed

Formatted: Space After: 0 pt

Formatted: Space After: 0 pt

Data availability

All data used in this publication are freely available on the Canada-Alberta Oil Sands Environmental Monitoring Information Portal: https://www.canada.ca/en/environment-climate-change/services/oil-sands-monitoring/monitoring-air-quality-alberta-oil-sands.html

Acknowledgements:

The authors thank the National Research Council of Canada flight crew of the Convair-580, the Air Quality Research Division technical support staff, Julie Narayan for in-field data management support, and Stewart Cober for the management of the study. The project was funded by the Air Quality program of Environment and Climate Change Canada and the Oil Sands Monitoring (OSM) program. It is independent of any position of the OSM program.

The authors declare no competing interests.